Available online at www.sciencedirect.com
ScienceDirect
Acta Materialia 59 (2011) 421–428
Acta MATERIALIA
www.elsevier.com/locate/actamat

Real-time control of AlN incorporation in epitaxial $Hf_{1-x}Al_xN$ using high-flux, low-energy (10–40 eV) ion bombardment during reactive magnetron sputter deposition from a $Hf_{0.7}Al_{0.3}$ alloy target

B.M. Howe [a], E. Sammann [a], J.G. Wen [a], T. Spila [a], J.E. Greene [a], L. Hultman [b], I. Petrov [a,*]

[a] Department of Materials Science and the Frederick Seitz Materials Research Laboratory, University of Illinois, 104 South Goodwin Avenue, Urbana, IL 61801, USA
[b] Department of Physics, Chemistry and Biology, Linköping University, SE-581 83 Linköping, Sweden

Received 18 July 2010; received in revised form 15 August 2010; accepted 18 August 2010
Available online 9 October 2010

Abstract

The AlN incorporation probability in single crystal $Hf_{1-x}Al_xN(0\,0\,1)$ layers is controllably adjusted between ~0% and 100% by varying the ion energy (E_i) incident at the growing film over a narrow range, 10–40 eV. The layers are grown on MgO(0 0 1) at 450 °C using ultrahigh vacuum magnetically unbalanced reactive magnetron sputtering from a $Hf_{0.7}Al_{0.3}$ alloy target in a 5%-N_2/Ar atmosphere at a total pressure of 20 mTorr (2.67 Pa). The ion to metal flux ratio incident at the growing film is constant at 8. Epitaxial film compositions vary from $x = 0.30$ with $E_i = 10$ eV, to 0.27 with $E_i = 20$ eV, 0.17 with $E_i = 30$ eV, and $\leqslant 0.002$ with $E_i \geqslant 40$ eV. Thus, the AlN incorporation probability decreases by greater than two orders of magnitude. This extraordinary range in real-time manipulation of film chemistry during deposition is due to the efficient resputtering of deposited Al atoms (27 amu) by Ar^+ ions (40 amu) neutralized and backscattered from heavy Hf atoms (178.5 amu) in the film. This provides a new reaction pathway to synthesize, at high deposition rates, compositionally complex heterostructures, multilayers, and superlattices with abrupt interfaces from a single alloy target by controllably switching E_i. For multilayer and superlattice structures, the choice of E_i value determines the layer composition and the switching periods control the individual layer thickness.
Published by Elsevier Ltd. on behalf of Acta Materialia Inc.

Keywords: Sputter deposition; Ion bombardment; Transition metal nitrides; HfAlN; Nanolayers

1. Introduction

Transition metal (TM) nitrides are well known for their remarkable physical properties, including high hardness and mechanical strength, chemical inertness, and electrical resistivity which varies from metallic to semi-conducting. Recently, the introduction of complexity into metastable transition metal nitride ceramic coatings in order to tailor their properties to specific applications has become an active area of research. The physical properties of nanocrystalline solids [1] are quite different from those of bulk large grained materials and depend strongly on crystallite size and shape. Multicomponent [2–5], multiphase [6–11], 2-dimensional [12–14], and 3-dimensional nanostructured hard coatings [15–17] have been synthesized with extreme properties, such as ultrahardness and ultratoughness [5,7–9,18,19], high ductility [20,21], and ultra wear resistance [22].

We have used metastable $Hf_{1-x}Al_xN$ alloys as a model system to investigate low energy ion-induced nanostructure formation in epitaxial NaCl structure TM nitrides [23]. HfN exhibits relatively high hardness among the binary

* Corresponding author. Tel.: +1 217 333 8396; fax: +1 217 244 2278.
E-mail address: petrov@illinois.edu (I. Petrov).

1359-6454/$36.00 Published by Elsevier Ltd. on behalf of Acta Materialia Inc.
doi:10.1016/j.actamat.2010.08.023

TM nitrides (25 GPa) [24]. We have shown that epitaxial metastable $Hf_{1-x}Al_xN$ alloys can be grown with x up to 0.5. At $x \geqslant 0.54$ they are fine grained mixtures of hexagonal wurtzite structure AlN and cubic HfN. Epitaxial layers with $0.3 \leqslant x \leqslant 0.5$ exhibit an equiaxed spinodal nanostructure consisting of HfN- and cubic AlN-rich domains, $\simeq$1.5 nm in diameter, corresponding to a 50% increase in hardness [23].

Here we investigate the effect of low energy ($E_i = 10$–40 eV) ion irradiation during film growth on the composition and nanostructure of $Hf_{1-x}Al_xN(0\,0\,1)$ layers grown from a $Hf_{0.7}Al_{0.3}$ alloy target. Epitaxial film compositions vary from $x = 0.3$ with $E_i = 10$ eV, to 0.27 with $E_i = 20$ eV, 0.17 with $E_i = 30$ eV, and $\leqslant$0.002 with $E_i \geqslant 40$ eV. This remarkably large change in AlN incorporation probability (more than two orders of magnitude) provides a novel and robust reaction pathway for synthesizing, at high deposition rates, compositionally complex heterostructures, multilayers, and superlattices, with abrupt interfaces, from a single metal HfAl alloy target by controllably switching E_i.

2. Experimental procedure

All $Hf_{1-x}Al_xN$ layers are grown in a load locked multichamber ultrahigh vacuum (UHV) system described in detail by Petrov et al. [25]. The pressure in the sample introduction chamber is reduced to less than 5×10^{-8} Torr (7×10^{-6} Pa), using a 50 l s^{-1} turbo-molecular pump (TMP), prior to initiating substrate exchange into the deposition chamber, which has a base pressure of 5×10^{-10} Torr (7×10^{-8} Pa), achieved using a 500 l s^{-1} TMP. The target is a 7.62 cm diameter water-cooled $Hf_{0.7}Al_{0.3}$ alloy disk (99.9% purity, excluding 3% Zr, the usual impurity in Hf) obtained from Plansee SE (Austria). Film growth is carried out in magnetically unbalanced mode [25] at a constant power of 100 W and total pressure of 20 mTorr (2.67 Pa) in 5% N_2/Ar mixed atmospheres (99.999% and 99.9999% pure N_2 and Ar, respectively) with a target to substrate distance of 6 cm, resulting in an alloy deposition rate of 0.53 nm s^{-1} on grounded substrates. The relatively high pressure is used to thermalize sputtered atoms and the majority of ions neutralized and reflected from the target [26]. Thus, the primary energetic particles incident at the growing film are ions attracted by the substrate bias. Rutherford backscattering spectroscopy (RBS) measurements show that the composition of films deposited on grounded substrates is $Hf_{0.7}Al_{0.3}N$, with an Al/Hf ratio equal to that of the target.

A combination of Langmuir probe [25], deposition rate, and film composition measurements reveal that the ion to metal ratio J_i/J_{Me} incident at the growing film remains constant at 8 and is not a function of E_i over the entire range investigated here, 10–80 eV. Ion irradiation of the growing film is essentially mono-energetic since the charge exchange mean free path [27] is more than an order of magnitude larger than the substrate sheath width [28]. Moreover, based upon glow discharge mass spectroscopy experiments carried out under similar reactive sputtering conditions, the composition of ions incident on the substrate is predominantly Ar^+ (>95%) with $\sim$4% Ar^{2+}, the remainder, <1% being metal target ions, N^+, and N_2^+ [29].

The substrates are polished $10 \times 10 \times 0.5\ mm^3$ MgO(0 0 1) wafers which are cleaned and degreased by successive rinses in ultrasonic baths of trichloroethane, acetone, methanol, and deionized water and blown dry in dry N_2. Final substrate cleaning consists of thermal degassing under vacuum at 800 °C for 1 h, a procedure shown to result in sharp MgO(0 0 1)1 × 1 reflection high energy electron diffraction patterns [30]. Immediately prior to initiating deposition, the target is sputter etched for 5 min with a shutter shielding the substrate. All layers are grown at $T_s = 450$ °C ($T_s/T_m \lesssim 0.2$, where T_m is the melting point of HfN in K), which includes the contribution due to plasma heating. This, as shown previously, results in epitaxial $Hf_{1-x}Al_xN(0\,0\,1)$ layers [23].

The compositions of the as-deposited multilayers are determined by 2 MeV He^+ RBS in which the spectra are analyzed using the SIMNRA simulation program [31]. Relative AlN concentrations as a function of depth through multilayer samples are determined by dynamic secondary ion mass spectrometry (SIMS) using a Cameca ims 5f operated with a 12.5 kV O_2^+ primary beam while collecting Al^+ ions. Samples grown on grounded substrates, with composition $Hf_{0.7}Al_{0.3}N$ (as determined by RBS), are used as a standard for SIMS depth profile analyses.

The nanostructure, phase composition, and texture of the as-deposited films are investigated using X-ray diffraction (XRD), high resolution reciprocal lattice mapping (HR-RLM), cross-sectional TEM (XTEM), high resolution XTEM (HR-XTEM) and high resolution Z-contrast scanning TEM (HR-STEM). XRD 2θ–ω scans are carried out in a Philips X'pert MRD diffractometer system using CuK_α radiation ($\lambda = 0.154180$ nm) with a Ni filter to remove CuK_β reflections and thin film parallel plate collimator secondary optics. HR-RLM images are acquired in a separate Philips X'pert MRD diffractometer using CuK_α 1 ($\lambda = 0.154056$ nm) radiation in line focus. The primary optics consist of a parabolic mirror and a two-reflection Ge monochromator, while a high speed line detector serves as the secondary optics.

HR-STEM images are acquired using a JEOL 2010F scanning/transmission electron microscope and a JEOL 2200FS instrument equipped with a probe aberration corrector (CEOS GmbH, Heidelberg, Germany). The lateral resolution of the JEOL 2200FS used for high angle annular dark field (HAADF) imaging is approximately 0.1 nm [32]. XTEM Z-contrast images are acquired by scanning a 0.1 nm probe across a specimen and recording the transmitted high angle incoherently scattered electrons with an annular detector (inner angle >100 mrad). Under these conditions, the image intensity I is accurately described as a convolution between the electron probe and an object function sharply peaked at the positions of each atomic column. At constant film thickness, I is a monotonic function of the

mean square atomic number (Z) of the column; i.e. I increases with increasing Z.

The effect of E_i on the composition and nanostructure of reactively sputter deposited $Hf_{1-x}Al_xN(0\,0\,1)$ films is investigated by growing multilayers in which E_i is sequentially varied in 10 eV steps from 10 to 80 eV, each sublayer grown for 120 s. For reference, separate 0.5-μm-thick $Hf_{1-x}Al_xN(0\,0\,1)$ layers are also deposited at each E_i value.

RBS measurements show that all $Hf_{1-x}Al_xN$ layers are slightly over-stoichiometric, N/(Hf Al) = 1.03 ± 0.05.

3. Experimental results

A typical RBS spectrum from an eight layer sample in which E_i is varied from 10 to 80 eV in steps of 10 eV is presented in Fig. 1a. The dominant feature is the Hf peak which appears at high backscattering energies due its high atomic number. The peak has a two-step structure (1.31–1.53 and 1.53–1.82 MeV) in which the higher-energy, higher-intensity region corresponds to an elevated HfN concentration. To first order, the bimodal peak shape is well fit by a $Hf_{1-x}Al_xN$ composition of $x = 0.30$ for the bottom three layers ($E_i = 10$, 20, and 30 eV) and $x = 0$ for the top five layers ($E_i = 40$, 50, 60, 70, and 80 eV). Higher resolution results are presented below.

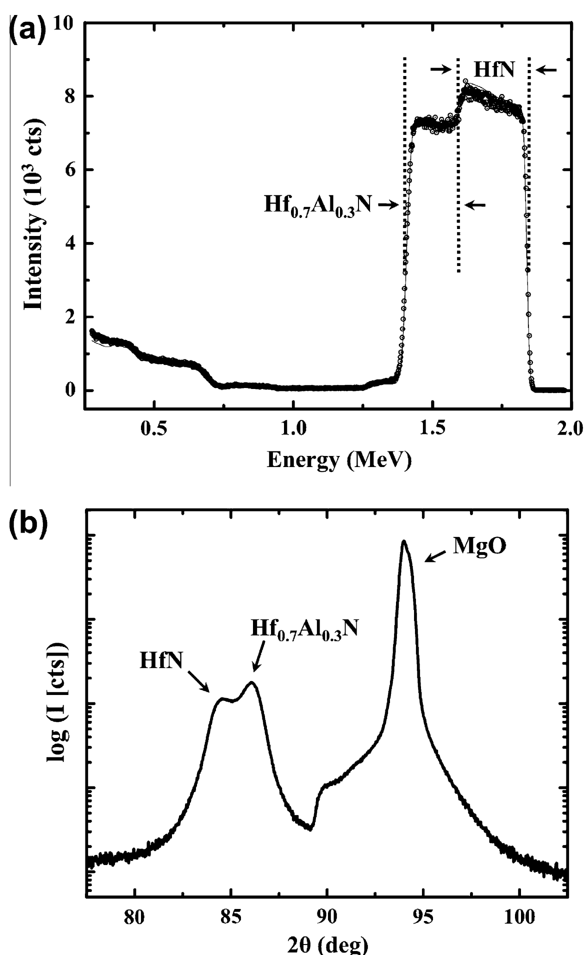

Fig. 1. (a) Rutherford backscattering spectrometry profile of an eight layer $Hf_{1-x}Al_xN$ film grown by varying the E_i from 10 to 80 eV in 10 eV increments. The deposition time for each layer is 120 s. (b) A narrow section of an ω–2θ X-ray diffraction scan ($2\theta = 10$–100°) from the multilayer film corresponding to (a). Only 0 0 2 and 0 0 4 film and substrate peaks are observed over the entire 2θ range.

The E_i-dependent deposition rates can be determined using data obtained from the RBS results and the deposition time for each layer. The total area under the Hf two-peak feature corresponds to 1.26×10^{18} atoms cm^{-2}, while the atomic areal densities of the two individual peaks are 4.8×10^{17} atoms cm^{-2} in the bottom three layers (with $E_i = 10$–30 eV) and 7.8×10^{17} atoms cm^{-2} in the upper five layers (with $E_i = 40$–80 eV), corresponding to incorporated Hf fluxes (J_{Hf}) of 1.33×10^{15} and 1.30×10^{15} cm^{-2} s^{-1}, respectively. This is in reasonable agreement with the value $J_{Hf} = 1.39 \times 10^{15}$ cm^{-2} s^{-1} expected from the multilayer deposition rate $R = 0.325$ nm s^{-1}, calculated assuming fully dense films with lattice constants obtained by XRD (see discussion below) and neglecting the slight N overstoichiometry. The incorporated Al flux in the bottom three layers, as determined by RBS analyses of multilayer samples, is $J_{Al} = 5.7 \times 10^{14}$ cm^{-2} s^{-1}, resulting in $Hf_{1-x}Al_xN$ layers with $x = 0.3$. Thus, by RBS analysis, the AlN incorporation probability $\sigma_{AlN} \approx 1$ for $E_i = 10$–30 eV, while $\sigma_{AlN} \approx 0$ with $E_i \geqslant 40$ eV (more accurate results are presented below). The HfN incorporation probability remains approximately constant at unity ($\sigma_{HfN} \approx 1$) over the entire range of E_i, 10–80 eV.

Fig. 1b is a section of an XRD 2θ–ω scan ($2\theta = 10$–110°) from the same multilayer sample. The only features observable over the entire 2θ range are the 0 0 2 and 0 0 4 substrate and film peaks. No peaks are obtained in glancing angle scans (not shown here) throughout the same 2θ range, indicating that the films are single-phase epitaxial NaCl structure layers. The $Hf_{1-x}Al_xN(0\,0\,2)$ reflection in Fig. 1b exhibits a pronounced splitting with peaks corresponding to interplanar spacings d_{002} of 0.2290 and 0.2257 nm, in agreement with previously reported d_{002} values of 0.227 nm for HfN and 0.2253 nm for $Hf_{0.69}Al_{0.31}N$ single crystal layers, respectively [23].

A typical HR-RLM about asymmetric $\bar{1}\bar{1}3$ reflections is shown in Fig. 2 for the $Hf_{1-x}Al_xN(0\,0\,1)$ film, with E_i varied from 10 to 80 eV in 10 eV steps, discussed above. Diffracted intensity distributions are plotted as isointensity contours as a function of the reciprocal lattice vectors $k_{\parallel}$ parallel and $k_{\perp}$ perpendicular to the surface. $k_{\parallel}$ and $k_{\perp}$ are related to peak positions in ω–2θ space through the relationships [33],

$$k_{\parallel} = 2r_E \sin(\theta)\cos(\omega - \theta) \quad (1)$$

and

$$k_{\perp} = 2r_E \sin(\theta)\sin(\omega - \theta), \quad (2)$$

where r_E is the Ewald sphere radius given by $r_E = 1/\lambda$. For a $\bar{1}\bar{1}3$ reflection from an 0 0 1 oriented NaCl-structure sample the in-plane $a_{\parallel}$ and out-of-plane $a_{\perp}$ lattice parameters

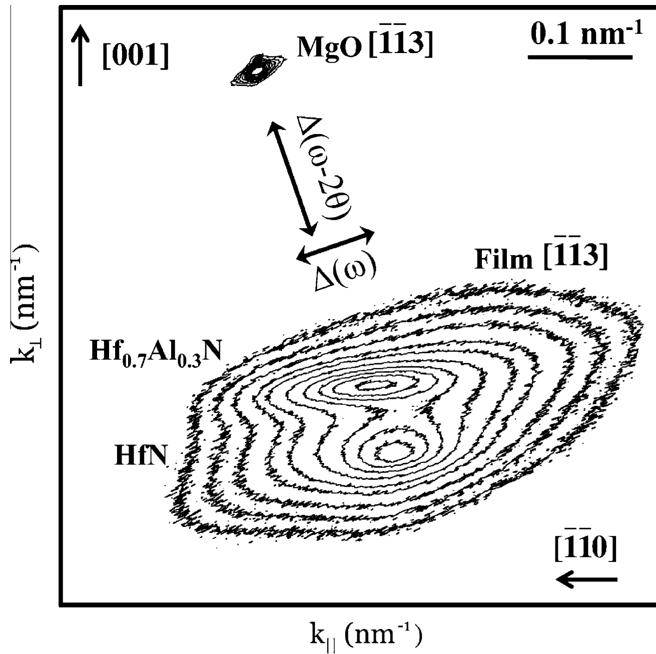

Fig. 2. HR-RLMs about the asymmetric $\bar{1}\bar{1}3$ reflections of an eight layer $Hf_{1-x}Al_xN$/MgO(0 0 1) film in which E_i is varied in 10 eV steps from 10 to 80 eV.

are given by $a_{||} = \sqrt{2}/k_{||}$ and $a_{\perp} = 3/k_{\perp}$. Relaxed bulk $Hf_{1-x}Al_xN$(0 0 1) lattice constants a_o are determined from $a_{||}$ and $a_{\perp}$ values through the relationship

$$a_o = a_{\perp}\left(1 - \frac{2v(a_{\perp} - a_{||})}{a_{||}(1+v)}\right), \quad (3)$$

where v is the film Poisson ratio. The residual in-plane strain $\varepsilon_{||}$ is defined as:

$$\varepsilon_{||} = \frac{a_{||} - a_o}{a_o}. \quad (4)$$

The fact that the substrate and layer peaks in Fig. 2 are misaligned along $k_{||}$ indicates the presence of in-plane strain relaxation. All layers are found to be nearly fully relaxed at the growth temperature and contain a small amount of residual compressive strain $\varepsilon_{||}$, ranging from −0.8% for $Hf_{0.7}Al_{0.3}N$(0 0 1) to −1.1% for HfN(0 0 1), which is primarily accounted for by differential thermal contraction during sample cooling following deposition.

The vertical separation between the film and substrate diffracted intensity distributions in Fig. 2 corresponds to a lattice mismatch in the growth direction of 7.13% for $Hf_{0.7}Al_{0.3}N$(0 0 1) and 8.76% for HfN(0 0 1), yielding out-of-plane lattice parameters $a_{\perp} = 0.4512$ nm ($Hf_{0.7}Al_{0.3}N$(0 0 1)) and $a_{\perp} = 0.4581$ nm (HfN(0 0 1)). The in-plane $Hf_{0.7}Al_{0.3}N$ lattice parameter $a_{||}$ is 0.4454 nm, while that of HfN(0 0 1) is 0.4496 nm. Substituting these values, together with a Poisson ratio of 0.25, into Eq. (3) yields a relaxed lattice constant a_o of 0.4489 nm for $Hf_{0.7}Al_{0.3}N$ and 0.4547 nm for HfN. While the Poisson ratio v for $Hf_{1-x}Al_xN$ is unknown, v values for related cubic TM nitrides only vary from 0.211 for TiN [34] to 0.29 for CrN [35]. We choose an average value of 0.25 to determine the relaxed lattice constant a_o of $Hf_{1-x}Al_xN$. The uncertainty in a_o introduced by v_{HfAlN} is ± 0.00002 nm (±0.004%). Moreover, the a_o results are in agreement with previously reported values for $Hf_{1-x}Al_xN$ grown on MgO(0 0 1) by reactive magnetron sputtering from separate elemental Hf and Al targets [23].

Fig. 3a is a typical XTEM bright field image from the multilayer $Hf_{1-x}Al_xN$(0 0 1) sample corresponding to Figs. 1 and 2. The total film thickness is 360 nm; the lower, brighter contrast region is 165 nm and the upper, darker contrast region is 195 nm thick. The interface corresponds to the boundary between the $E_i = 30$ eV and 40 eV layers; the average thickness of the bottom three $Hf_{1-x}Al_xN$ layers is 55 nm, while the upper five HfN layers are 39 nm each. The ratio of deposition rates of the upper and lower layers is 0.71 (in good agreement with the RBS results). Combining this with the RBS compositional data provides an AlN

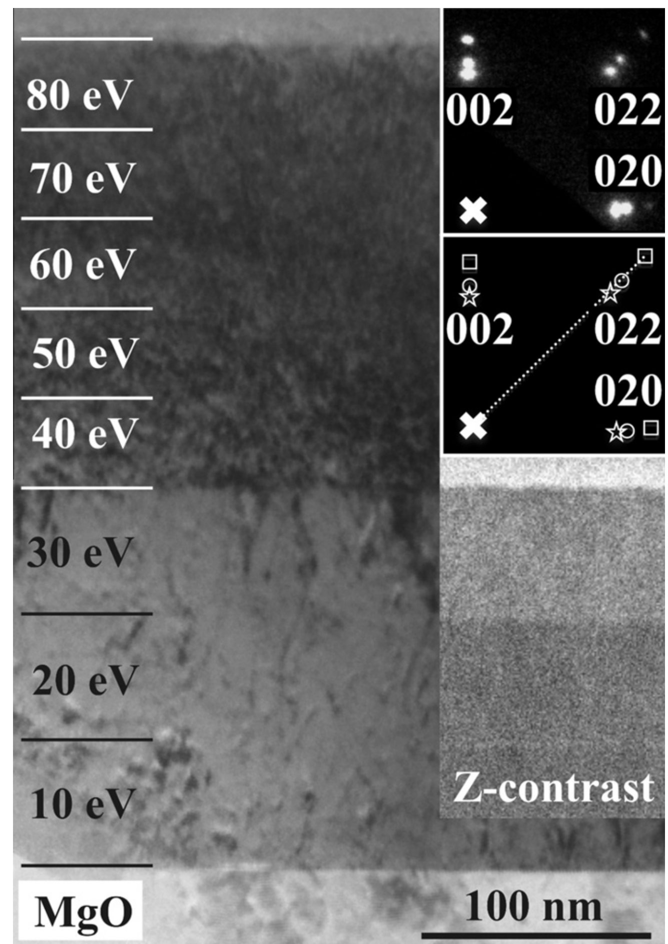

Fig. 3. A bright field XTEM image from an eight layer $Hf_{1-x}Al_xN$ film in which E_i is varied in 10 eV steps from 10 to 80 eV. The upper right inset is a selected area electron diffraction pattern including contributions from both the film and substrate. The middle inset is a schematic diagram of the diffraction peaks. The symbol x denotes the transmitted beam position, while the squares, circles, and stars correspond to the substrate, the upper ($E_i = 40$–80 eV) portion of the film, and the lower ($E_i = 10$–30 eV) portion of the film, respectively. The lower right inset is a Z-contrast image for $E_i = 10$, 20, 30, and 40 eV layers.

incorporation probability $\sigma_{AlN} \approx 1$ in the lower three layers and ≈0 in the upper layers, with $\sigma_{HfN} \approx 1$ throughout.

The weak intensity variations along the growth direction of the brighter contrast lower three layers are due to diffraction contrast induced by the presence of threading dislocations, which are clearly resolved when examining thinner cross-sectional specimens. The darker contrast in the upper portion of the film is due to a combination of two effects: (1) decreased AlN incorporation giving rise to stronger electron-beam absorption by the higher atomic number Z component HfN and (2) local strain contrast arising from residual ion irradiation-induced defects as the interaction volume of the incoming ions increases with increasing $E_i > 40$ eV.

The upper right inset of Fig. 3 is an SAED pattern obtained with the electron beam sampling a total thickness of 400 nm, including the full thickness of the multilayer film and a small portion of the substrate. The 0 0 2, 0 2 2 and 0 2 0 reflections are split with three distinct spots corresponding to HfN (innermost), $Hf_{1-x}Al_xN$ (middle) and the MgO substrate (outermost), as shown in the schematic inset in Fig. 3. The positions of the 0 0 2 peaks agree with the XRD results in Fig. 1. The 0 2 2 SAED reflections are aligned with the transmitted beam, i.e. the multilayer film is fully relaxed, as confirmed by the HR-RLM results in Fig. 2. These results, together with XRD ϕ scans about asymmetric (2 2 0) peaks (not presented here), show that the film grows epitaxially with a cube-on-cube orientational relationship to the substrate: $(0\,0\,1)_{HfAlN}\|(0\,0\,1)_{MgO}$ and $[1\,0\,0]_{HfAlN}\|[1\,0\,0]_{MgO}$.

The lower right inset of Fig. 3 is a Z-contrast STEM image focused on the bottom four layers for which $E_i = 10$, 20, 30, and 40 eV. The local image brightness is proportional to the average atomic number Z. The first two layers ($E_i = 10$ and 20 eV) have approximately equal intensities, indicating a nearly constant alloy composition (note that the sharp bright boundary between the two layers was due to a slight overshoot in the bias voltage during manual adjustment). However, layer three ($E_i = 30$ eV) is noticeably brighter, indicating a substantial decrease in the AlN incorporation probability. σ_{AlN} is even lower in the much brighter $E_i = 40$ eV layer, for which RBS and XRD results show that the AlN incorporation probability is near 0. The Z-contrast intensity does not vary with further increases in E_i, i.e. the brightnesses of the $E_i = 40$, 50, 60, 70, and 80 eV layers are indistinguishable.

The observed decrease in σ_{AlN} with increasing E_i is quantified using SIMS. A 0.5-μm-thick $Hf_{0.7}Al_{0.3}N(0\,0\,1)$ film, verified by RBS, grown with $E_i = 10$ eV serves as an internal composition standard. A typical SIMS profile of the Al distribution through a $Hf_{1-x}Al_xN(0\,0\,1)$ multilayer is presented in Fig. 4 on a logarithmic scale, as well as two linear plots of the $E_i = 10$–40 eV and 40–80 eV regions. The measured layer compositions are: $x = 0.3000$ ($E_i = 10$ eV), $x = 0.2700$ ($E_i = 20$ eV), $x = 0.1700$ ($E_i = 30$ eV), $x = 0.0020$ ($E_i = 40$ eV), $x = 0.0015$ ($E_i = 50$ eV), $x = 0.0025$ ($E_i = 60$ eV) and $x = 0.0032$ ($E_i = 70$ and 80 eV). The Al detection limit, estimated from the signal intensity at the Al^+ peak position obtained from the MgO substrate, is more than two orders of magnitude lower than the minimum Al^+ signal from the film.

Thus, σ_{AlN} decreases from unity at $E_i = 10$ eV by a factor of ~150 times at $E_i = 40$ eV to ~200 times at $E_i = 50$ eV, while σ_{HfN} remains constant at unity over the E_i energy range, 10–80 eV. This trend is depicted in

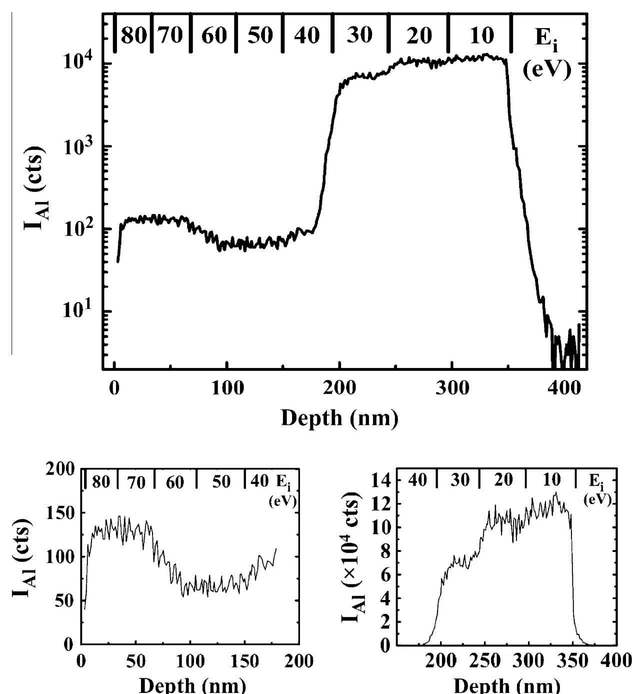

Fig. 4. SIMS Al depth profile through an eight layer $Hf_{1-x}Al_xN$ film in which E_i was varied from 10 to 80 eV in 10 eV increments. The profile was obtained using a 12.5 kV O_2^+ primary beam while collecting sputter-ejected Al^+ ions. The insets below are linear plots over the E_i ranges 10–40 and 40–80 eV.

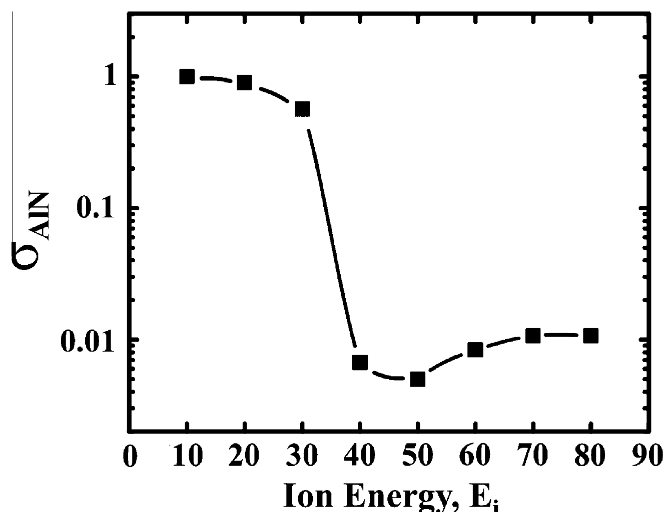

Fig. 5. The AlN incorporation probability vs. ion energy E_i obtained from SIMS depth profiles through an eight layer $Hf_{1-x}Al_xN$ film in which E_i is varied from 10 to 80 eV in 10 eV increments.

Fig. 5 as a plot of σ_{AlN} vs. E_i. The dramatic decrease in σ_{AlN} between $E_i = 30$ and 40 eV is clearly observed.

4. Discussion

The dramatic decrease in the AlN incorporation probability with increasing E_i is not due to target effects. At steady-state, the composition of sputtered species from an alloy target is equal to the target composition [36]. Furthermore, at the deposition temperature used in these experiments, $T_s = 450\,°C$ ($T_s/T_m \gtrsim 0.2$), the sticking probability of the metallic species arriving at the growth front is essentially unity. Finally, at the gas phase pressure used in these experiments, 20 mTorr, the thermalization distances of sputtered Al and Hf atoms and Ar^+ ions neutralized and reflected from the target is <20 mm [26], while the target to substrate separation is 60 mm. The primary energetic species incident at the growing film are Ar^+ with energies $E_i = eV_s$, where $V_s = (V_{plasma} - V_a)$, in which V_{plasma} is the plasma potential and V_a is the applied substrate potential. Therefore, $\sigma_{AlN}(E_i)$ is controlled solely by low energy ion/atom interactions in the growing film surface region.

Berg and Kartadjiev have modeled dynamic preferential resputtering of lighter mass components from a growing alloy film due to ion bombardment during deposition [37]. The term "sputter yield amplification" (SYA) was coined to describe the compositional enhancement of a higher mass m_h solute element with respect to the lower mass m_l solvent element due to bombardment by intermediate mass m_i ions. Simulations were carried out using a dynamic version of TRIM [38], T-DYN [39], to calculate the resputtering yields of C or Al (12 and 27 amu, respectively) by 300–1000 eV inert gas ions (Ar^+ and Xe^+, 40 and 131 amu, respectively) in the presence of various solute elements ranging across the periodic table.

Enhancement of the Al resputtering yield by up to a factor of five was demonstrated upon addition of a few atomic percent of W (184 amu) or Pt (195 amu). The effect is primarily due to the increased directional isotropy of the incident ion momentum which occurs when adding higher mass solute atoms to lighter mass film atoms. The same is true for recoiled knock-on host atoms. Both effects result in shorter ion ranges and denser cascades. Moreover, a significant fraction of incident ions which penetrate the growing film are reflected from higher mass solute atoms towards the surface. The net result is an increased dynamic sputter yield (loss) of the lighter component during alloy film deposition. For co-deposition of Al and W, a materials system analogous to the one studied, simulations show that the Al/W ratio decreases from five in the absence of ion irradiation to ~0.45 with concurrent $E_i = 500$ eV Ar^+ bombardment during film growth. That is, the ratio Al/W in the incident beam to that in the as-deposited layer decreases by a factor of ~11 as E_i increases from 0 to 500 eV.

While the trends observed in our experiments are in general agreement with the SYA model, the magnitude is completely unexpected when considering the very low E_i values: the AlN content in $Hf_{1-x}Al_xN$ films varies by a factor of ~200 times over a small E_i range, 10–50 eV. There are several factors that account for the extraordinarily large SYA effect observed here. Our experiments are carried out near the threshold of sputtering, far from the linear cascade regime. Moreover, we employ reactive sputtering of nitrides, which have much higher cohesive energies U_s than pure metals, thus strongly affecting sputtering rates in the threshold regime. Cohesive energies computed by first principle density functional theory (DFT) calculations are $U_s = 11.4$ eV for AlN and 10.4 eV for HfN (B. Jansson, unpublished), while experimental values for Al and Hf are $U_s = 3.39$ and 8.90 eV, respectively [40]. Finally, we employ a very high ion to metal flux ratio, $J_i/J_{Me} = 8$, compared with a typical value of 0.3 from Berg and Kartadjiev.

Further examination of the atomistic collisions taking place in the near surface regions during ion-assisted film growth, i.e. within the first few atomic layers, helps to explain this unique phenomenon. Let us first consider energy transfer to film atoms from an impinging Ar^+ ion. The ion undergoes maximum energy transfer during 180° backscattering collisions. For a hard sphere elastic collision between an Ar^+ ion and a Hf atom, the energy transfer can be estimated as $4m_{Hf}m_{Ar}/(m_{Hf} + m_{Ar})^2E_i$ [41]. That is, approximately $0.6E_i$ is transferred to Hf and, hence, the Ar is backscattered with energy $E_b \approx 0.4E_i$. However, an energetic Ar^+ ion encountering an Al atom in a head-on collision transfers ~97% of its energy and is reflected back toward the surface with E_b of only ~$0.03E_i$. Thus, the direct pathway of selective Al resputtering is the simple sequence of an ion backscattered from a Hf atom followed by collision with an Al atom on the way out.

The reflection coefficient, based on TRIM calculations, of Ar^+ impinging on a Hf surface atom is ~0.25. With $J_i/J_{Me} = 8$, each deposited atom is, on average, struck by several energetic reflected ions. This energy is transferred extremely efficiently to Al atoms (~97%) and less efficiently to Hf atoms (~60%). With $Hf_{1-x}Al_xN$ cohesive energies of ~10 eV there is a window of E_b energies for which Al is resputtered preferentially due to more efficient momentum transfer, while E_b remains near or below the Hf sputtering threshold. N atoms will also be efficiently reflected in the backward direction. However, due to the substantial N_2 partial pressure, excess N is continually supplied to the growth surface via collisionally-induced N_2^+ dissociation.

A unique and positive aspect of achieving compositional control during film growth at near threshold ion irradiation energies (10–40 eV) is the lack of significant Ar trapping or residual ion-induced damage, as indicated by the XRD and HR-RLM results showing very low compressive stress. SIMS results indicated a slight increase in AlN content from $x = 0.0015$ to 0.0025 at $E_i > 60$ eV, which can be attributed to the onset of forward Al scattering by incoming Ar^+ ions.

We apply this extraordinary SYA threshold effect to synthesize epitaxial $Hf_{1-x}Al_xN$/HfN superlattices by sequentially alternating E_i values. An example is shown in Fig. 6 in which a 50-nm-thick $Hf_{0.7}Al_{0.3}N$ buffer layer

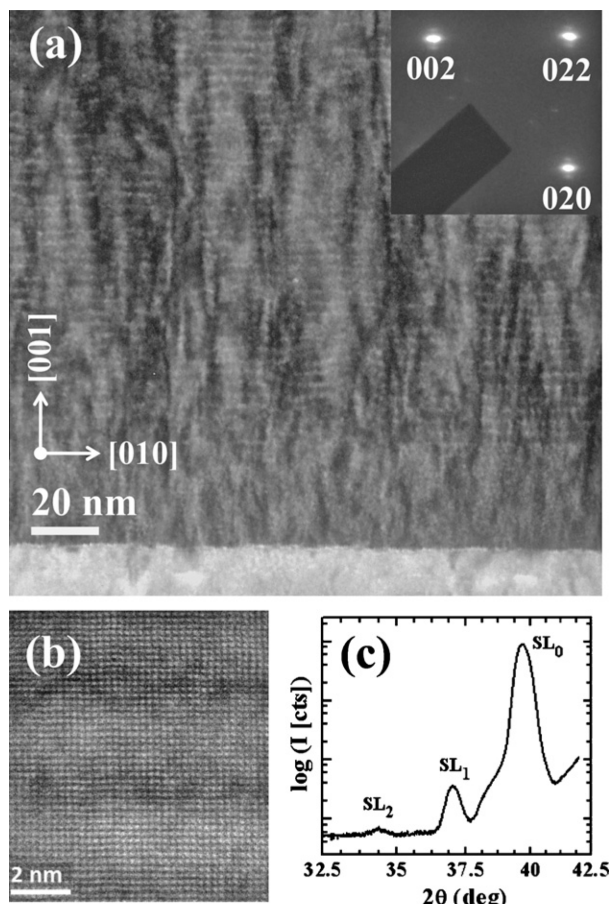

Fig. 6. (a) A [1 0 0] zone axis XTEM image of an epitaxial $Hf_{0.7}Al_{0.3}N$/HfN superlattice grown on a 50-nm-thick $Hf_{0.7}Al_{0.3}N$ buffer layer on MgO(0 0 1) by sequentially varying the ion energy E_i incident at the growing film between 10 and 40 eV during reactive magnetron sputter deposition from a $Hf_{0.7}Al_{0.3}$ alloy target. The inset is a selected area electron diffraction pattern revealing satellite peaks in the growth direction resulting from the imposed 2D nanostructure. (b) A [1 0 0] zone axis high resolution Z-contrast image (showing atomic column contrast). (c) The X-ray diffraction pattern about the 0 0 2 film peak SL_0 revealing satellite reflections SL_1 and SL_2.

is first grown with $E_i = 10$ eV, followed by 120 $Hf_{0.7}Al_{0.3}N$/HfN(0 0 1) bilayers in which E_i is switched between 40 eV for 4 s and 10 eV for 3 s. The deposition times were chosen to provide equi-thick, 1.6 nm, layers. Dividing the total thickness of the superlattice film, as determined by XTEM, by the total number of bilayers, we obtain a bilayer period $\Lambda = 3.2$ nm, which is in excellent agreement with the positions of the SAED (inset, Fig. 6) and XRD (Fig. 6c) superlattice satellite reflections.

The multilayer films can be represented by a modulated compositional wave with period Λ, given by twice the layer thickness. Any arbitrary wave shape can be reproduced by a Fourier series of sine waves with increasing harmonic frequencies.

Diffraction theory [42,43] predicts satellite peaks at angles of $\theta_\pm$ about the Bragg reflection at θ_B, the Bragg angle for the average film composition. The angles $\theta_\pm$ are related to the X-ray wavelength λ and the compositional modulation period Λ by:

$$\sin\theta_\pm = \sin\theta_B \pm (\lambda/2)\Lambda. \quad (5)$$

A non-sinusoidal periodic function, such as a square wave, results in higher order satellites at increasing separation from θ_B. Substituting the values of $\theta_\pm$, θ_B, and λ from Fig. 6c into Eq. (5) we obtain an average superlattice bilayer thickness $\Lambda = 3.257$ nm, in good agreement with the experimental results.

The high resolution STEM image in Fig. 6b confirms that the superlattice is of high crystalline quality with no detectable dislocations. The Z modulation in the growth direction due to controlled manipulation of the AlN incorporation probability σ_{AlN} by modulating E_i between 10 and 40 eV during film growth is clearly resolved.

5. Conclusions

The AlN incorporation probability in single crystal $Hf_{1-x}Al_xN$(0 0 1) layers was controllably varied between ~0% and 100% by dynamically altering the energy E_i of Ar^+ and N_2^+ ions incident at the growing film over a narrow range, 10–40 eV, near the sputtering threshold. Epitaxial film compositions (and AlN incorporation probabilities σ_{AlN}) vary from $x = 0.3$ ($\sigma_{AlN} = 1$) with $E_i = 10$ eV to 0.27 ($\sigma_{AlN} = 0.9$) with $E_i = 20$ eV, 0.17 ($\sigma_{AlN} = 0.57$) with $E_i = 30$ eV to $\leqslant 0.002$ ($\sigma_{AlN} = 0.007$) with $E_i \geqslant 40$ eV. This extraordinary range in real-time manipulation of film chemistry during film deposition is due primarily to the efficient resputtering of Al atoms (27 amu) by Ar^+ ions (40 amu) backscattered from heavy Hf atoms (178.5 amu) in the film. The effect is used to grow planar nitride alloy heterostructures and superlattices with abrupt interfaces at high deposition rates from a single metal alloy target by controllably switching E_i. The choice of E_i value determines the layer composition, while the switching period controls the individual layer thickness.

Acknowledgements

This work was carried out in part in the Frederick Seitz Materials Research Laboratory Central Facilities, Center for Microanalysis of Materials, University of Illinois, which are partially supported by the US Department of Energy under Grants DE-FG02-07ER46453 and DE-FG02-07ER46471. B.M.H. gratefully acknowledges the support of the US Department of Defense Science, Mathematics, and Research for Transformation program. B.M.H., L.H., I.P. and J.E.G. also acknowledge support from a Swedish Government Strategic Research grant on Advanced Functional Materials, as well as the Swedish Research Council and Strategic Research Foundation.

References

[1] Gleiter H. Acta Mater 2000;48:1.
[2] Dobrzanski LA, Pakula D. Mater J Process Technol 2005;164/165:832.
[3] Subramanian C, Strafford KN. Wear 1993;165:85.

[4] Lee T-Y, Kodambaka S, Wen JG, Twesten RD, Greene JE, Petrov I. Appl Phys Lett 2004;84:2796.
[5] Adibi F, Petrov I, Hultman L, Wahlstrom U, Shimizi T, McIntyre D, et al. J Appl Phys 1991;69:6437.
[6] Musil J, Hruby H, Zeman P, Cerstvy R, Mayrhofer PH, Mitterer C. Surf Coat Technol 2001;603:142.
[7] Voevodin AA, Hu JJ, Fitz TA, Zabinski JS. Surf Coat Technol 2001;146:351.
[8] Zabinski JS, Donley MS, Dyhouse VJ, McDevit NT. Thin Solid Films 1992;214:156.
[9] Voevodin AA, Zabinski JS. Thin Solid Films 2000;370:223.
[10] Zehnder T, Patscheider J. Surf Coat Technol 2000;38:133.
[11] Bewilogua K, Cooper CV, Specht C, Schroder J, Wittorf R, Grischke M. Surf Coat Technol 2000;132:275.
[12] Barnett SA, Madan A. Scripta Mater 2004;50:739.
[13] Münz W-D. MRS Bull 2003;28:173–9.
[14] Cooke KE, Bamber M, Bassas J, Boscarino D, Derby B, Figueras A, et al. Surf Coat Technol 2003;162:276.
[15] Vepřek S, Vepřek-Heijman MGJ, Karvankova P, Prochazka J. Thin Solid Films 2005;476:1.
[16] Mayrhofer PH, Mitterer C, Wen JG, Greene JE, Petrov I. Appl Phys Lett 2005;86:1.
[17] Mayrhofer PH, Mitterer C, Greene JE, Petrov I. J Appl Phys 2006;100:044301.
[18] Vepřek S. J Vac Sci Technol A 1999;17:2401.
[19] Zehnder T, Patscheider J. Surf Coat Technol 2000;133:138.
[20] Vepřek S, Mukherjee S, Karvankova P, Männling H-D, He JL, Moto K. J Vac Sci Technol A 2003;21:532.
[21] McFadden SX et al. Nature 1999;398:684.
[22] Cao DM, Feng B, Meng WJ, Rehn LE, Baldo PM, Khonsari MM. Appl Phys Lett 2001;79:329.
[23] Howe B, Bareño J, Sardela M, Wen JG, Greene JE, Hultman L, et al. Surf Coat Technol 2007;202:809.
[24] Seo H-S, Lee T-Y, Wen JG, Petrov I, Greene JE. J Appl Phys 2004;96:878.
[25] Petrov I, Adibi F, Greene JE, Sproul WD, Munz W-D. J Vac Sci Technol A 1992;10:3283.
[26] Westwood WD. J Vac Sci Technol 1978;15:1.
[27] Phelps AV. J Phys Chem Ref Data 1991;20:557.
[28] Chapman B. Glow discharge processes. New York: Wiley; 1980.
[29] Petrov I, Myers A, Greene JE, Abelson JR. J Vac Sci Technol A 1994;12:2846.
[30] Powell RC, Lee N-E, Kim Y-W, Greene JE. J Appl Phys 1998;73:189.
[31] Mayer M. Nucl Instrum Methods B 2006;249:82.
[32] Wen J, Mabon J, Lei C, Burdin S, Sammann E, Petrov I, et al. Microsc Microanal 2010;16:183.
[33] van der Sluis P. J Phys D 1993;26:A188.
[34] Kim JO, Aschenbach JD, Mirkarimi PB, Shinn M, Barnett SA. J Appl Phys 1992;72:1805.
[35] Wiklund U, Bromark M, Larsson M, Hedenqvist P, Hogmark S. Surf Coat Technol 1997;91:57.
[36] Eltoukhy AH, Greene JE. J Appl Phys 1980;51:4444.
[37] Berg S, Katardjiev I. Surf Coat Technol 1996;84:353.
[38] Ziegler J, Biersack F, Littmark JP. The stopping and range of ions in solids, vol. 1. New York: Pergamon Press; 1985.
[39] Berg JP, Nender C. Nucl Instrum Methods B 1991;59/60:21.
[40] Anderson HH, Bay HL. In: Sputtering by particle bombardment. Berlin: Springer-Verlag; 1981.
[41] Behrisch R. Sputtering by particle bombardment: I. Physical sputtering of single-element solids. Berlin: Springer-Verlag; 1981.
[42] Guinier A. X-ray diffraction in crystals, imperfect crystals, and amorphous bodies. San Francisco: Freeman; 1963.
[43] de Fontaine D. In: Cohen JB, Hilliard JE, editors. Local arrangements studied by X-ray diffraction. New York: Gorden and Breach; 1967 (Chapter 2).